

Measuring Muon Neutrino
Disappearance With The NOvA
Experiment
Luke Vinton

Submitted for the degree of Doctor of Philosophy
University of Sussex
9th January 2017

Chapter 1

Introduction

The neutrino was discovered a little over 60 years ago and during the last two decades the ability of neutrinos to change flavour in flight has been established beyond doubt. The Standard Model of particle physics defines neutrinos to be massless. However, neutrino oscillations in vacuum requires that at least one of the neutrinos has a mass. This means that the current the model is incomplete and neutrino oscillations are beyond the Standard Model.

Neutrino oscillation experiments such as NOvA aim to measure the probability of a neutrino oscillating from one flavour to another and the rate of the oscillation. Such measurements probe the neutrino mixing angles and the difference between the squared neutrino masses.

the neutrino mixing parameters and the difference between

Chapter 2

Neutrino Physics

Let us start in 1914, when Chadwick presented experimental evidence [2] that the energy spectrum of electrons emitted in β decay was continuous instead of being discrete as expected. This meant either β decay was not a two-body process or conservation of energy was violated. The solution arrived in 1930, when neutrinos were postulated by Wolfgang Pauli [3] as a “desperate remedy” to the apparent non-conservation of energy in nuclear β decay. He suggested that an additional neutral and extremely light particle was produced in β decay which carried away the undetected energy. Pauli referred to this additional particle as a “neutron”. In 1934 Fermi [4] formulated a theory of β decay and re-named the additional particle as the “neutrino”.

In 1956, Cowan and Reines [5] incredibly overcame the hurdle of actually detecting neutrinos ¹ and provided the first direct evidence for their existence. They set up an experiment to measure the flux of neutrinos emitted from a nuclear reactor. The neutrinos from the reactor were produced via β decay and were detected via inverse β decay ($p + \bar{\nu} \rightarrow n + e^+$). If a neutrino interacted within the detector it would produce a characteristic signal of a pair of photons from electron-positron annihilation and a delayed photon from neutron capture.

At first it was thought that neutrinos only come in one flavour. This view changed with the subsequent discovery of muon and tau neutrinos. Muon and tau neutrinos were discovered several decades apart. In 1962 neutrinos which produce muons but not electrons when interacting with matter were observed [6]. In the paper it was suggested that neutrinos produced in association with a muon are muon neutrinos which are distinct from

¹They expressed the double edged sword of the validity of Pauli’s neutrino proposal and the difficulty of neutrino detection as “the very characteristic of the particle which makes the proposal plausible - it’s ability to carry off energy and momentum without detection”.

the electron neutrinos previously observed in β decay. In 1989, The ALEPH collaboration published measurements of the mass and width of the Z boson [7]. Consequently they were able to constrain the number of active light neutrinos to be three at 98% confidence level. Final results from the ALEPH experiment provided conclusive proof that the number of light active neutrinos is indeed three [8]. In 2000, the DONUT experiment reported an observation of four tau neutrino neutrinos with a background estimation of 0.34 events [9]. This third neutrino completed the set of the three standard model neutrinos associated with the three charged leptons.

The first hints of neutrino oscillations came from experiments measuring the flux of solar neutrinos. The Fusion reactions by which energy is produced in the sun are modelled by the Standard Solar Model. The model predicts three major neutrino emissions: pp neutrinos ($p + p \rightarrow d + e^+ + \nu_e$, $E_{max.} = 420$ keV), ${}^7\text{Be}$ neutrinos (${}^7\text{Be} + e^- \rightarrow {}^7\text{Li} + \nu_e$, $E_{max.} = 860$ keV) and ${}^8\text{B}$ neutrinos (${}^8\text{B} + e^- \rightarrow {}^8\text{Be} + e^+ + \nu_e$, $E_{max.} = 14$ MeV). [10] In 1968 Ray Davis et. al. published the “Search For Neutrinos From the Sun” paper [11]. In the same year Bahcall et. al. published a prediction for the solar neutrino flux experienced by Ray Davis’s experiment based on the standard solar model [12]. Davis used the interaction $Cl^{37} + \nu \rightarrow e^- + Ar^{37}$ to measure the flux of ${}^8\text{B}$ and ${}^7\text{Be}$ solar electron neutrinos. The measured rate of neutrinos was found to be only one third of the rate predicted by Bahcall. At the time of publication this discrepancy was generally attributed to errors in either the measurement technique or the standard solar model at high neutrino energies and became known as the “solar neutrino puzzle”. In 1989, the Kamiokande-II experiment confirmed the deficit of ${}^8\text{B}$ solar electron neutrinos relative to the standard solar model [13]. In 1991 and 1992, the deficit was further confirmed by two experiments, SAGE [14] and GALLEX [10], which both measured the rate of the less energetic pp solar neutrinos. These experiments showed that the flux deficit occurred for low energy pp neutrinos as well as the higher energy ${}^8\text{B}$ and ${}^7\text{Be}$ neutrinos measured previously.

Either the standard solar model was incorrect or electron neutrinos produced in the Sun do not all survive the journey to the Earth. Neutrino oscillation due to massive neutrinos became accepted as a realistic possibility. Previously, in the years 1962-1968, Pontecorvo, Maki, Nakagawa, and Sakata had formulated a theory including electron and muon neutrinos which were able to change from one to the other [15, 16, 17].

In 1998, Super Kamiokande reported evidence for the oscillation of atmospheric neutrinos [18]. They measured the rate of muon and electron neutrinos originating from collisions of cosmic rays with nuclei in the upper atmosphere. The detector allowed the reconstruc-

tion of the direction of the incoming neutrino, this revealed the baseline from production to detection and whether the neutrino travelled through the Earth. Electron and muon neutrinos are produced in the upper atmosphere in the ratio 1:2 (electron:muon). The asymmetry of upward and downward going events was measured for both electron and muon neutrinos. The electron neutrino asymmetry was consistent with zero but a momentum dependant asymmetry was observed for muon neutrinos at more than 6 standard deviations. The data was concluded to show evidence for neutrino oscillations.

In 2005, SNO published measurements of the flux of solar ^8B neutrinos [19]. They measured the rate of charged current electron neutrino events and were also able to measure the rate of neutral current events due to all three active neutrinos. The measured neutral current flux was consistent with the flux expected from the standard solar model but the measured flux of electron neutrinos was significantly lower than the measured total flux of active neutrinos. Neutrino oscillations were reconfirmed solving the solar neutrino puzzle.

Since the confirmation of neutrino oscillations the spotlight has moved on to the unknown neutrino properties, such as: the parameters which govern oscillations, the nature of neutrinos (whether they are Dirac or Majorana particles), strength of interaction with matter, the mass, origin of mass and the number of neutrinos. Experimental and theoretical advances have made progress on the above questions during the last ≈ 60 years [20] and the observation of neutrino oscillations has opened new fundamental questions regarding the origin of fermion masses and the relationship between quarks and leptons [21].

2.0.1 Recent results

The Kamioka Liquid Scintillator Anti-Neutrino Detectro (KamLAND) was designed as search for the oscillation of electron antineutrinos emitted from nuclear power stations. Typical baseline of 180 km intended to adress the oscillation solution to the “solar neutrino problem”. Use inverse β -decay to detect electron antineutrinos. 1 kton ultrapure LS detector. 2003, first evidence of electron antineutrino disappearance. Ratio of observed inverse β – decay events to expected events without electron neutrino disappearance was $0.611 \pm 0.085(\text{stat.}) \pm 0.041(\text{syst.})$. Fewer events than expected at the 99.95% confidence level. [22] 2005, direct evidence for neutrino oscillations via observation of distortion in rector electron antineutrino energy spectrum. [23] More recently in 2008. Exposure of 2.44×10^{32} proton yr Measured values: $\Delta m_{21}^2 = 7.58_{-0.13}^{+0.14}(\text{stat.})_{-0.06}^{+0.10}(\text{syst.})$ and $\tan^2 \theta_{12} = 0.56_{-0.07}^{+0.10}(\text{stat.})_{-0.06}^{+0.10}(\text{syst.})$. [24]

The Sudbury Neutrino Observatory (SNO) was created to measure the flux of neutrinos

produced in the Sun, by ^8B decays in particular. 1 kton detector. Imaging Cherenkov detector using heavy water ($^2\text{H}_2\text{O}$). 1.783 km below sea level and an overburden of 5.890 km water equivalent. SNO detected neutrinos via three processes: elastic scattering, charged current and neutral current interactions. Measuring the rates of these three processes gave insight on the overall flux of neutrinos from the sun and also the flux of electron neutrinos that reach the detector. By comparing these fluxes SNO was able to test the neutrino oscillation hypothesis. [25] In 2013. Combined result of SNO and all other solar and reactor neutrino experiments gave $\Delta m_{21}^2 = (7.46_{-0.19}^{+0.20}) \times 10^{-5} \text{ eV}^2$, $\tan^2 \theta_{12} = 0.443_{-0.025}^{+0.030}$ and $\sin^2 \theta_{13} = (2.49_{-0.32}^{+0.20}) \times 10^{-2}$. [26]

The Super Kamiokande (SK) is an imaging water Cherenkov detector designed to detect neutrinos produced by ^8B decays in the Sun. 2011 paper. Solar neutrino experiment measuring flux of electron neutrinos from the sun from the stellar production of neutrinos from the ^8B reaction chain. Via neutrino electron scattering. Located 1 km underground. 50 ktons of ultrapure water. signals read out by photomultiplier tubes. Three flavour fit produces $\sin^2 \theta_{12} = 0.30_{-0.01}^{+0.02}$ and $\Delta m_{21}^2 = 6.2_{-1.9}^{+1.1} \times 10^{-5} \text{ eV}^2$. In combination with other solar experiments and KamLand found $\sin^2 \theta_{13} = 0.025_{-0.016}^{+0.018}$. [27] [28]

Measurement of electron antineutrino disappearance with the Daya Bay experiment. Non zero value of θ_{13} measured with precision by Daya Bay, which measured $\sin^2 2\theta_{13} = 0.084 \pm 0.005$. Total exposure of $6.9 \times 10^5 \text{ GW}_{th} \text{ ton days}$. Opening the door to the measurement of electron neutrino appearance in a muon neutrino beam and hence measurements of the mass hierarchy and the CP violating phase δ_{CP} . Fully constructed experiment consists of 8 detectors and 6 nuclear reactor cores. [29] Large value of $\sin^2 \theta_{13}$ measured by Daya Bay [30].

RENO is a reactor antineutrino disappearance experiment. Reactor electron antineutrinos are detected via inverse β decay. Coincidence of prompt positron signal and a delayed photon signal from neutron capture is the signature for inverse β decay. Two identical detectors located 294 m and 1383 m from the centre of six reactor cores. Each detector consists of a main inner detector and an outer veto detector. $\sin^2 2\theta_{13} = 0.082 \pm 0.009(\text{stat.}) \pm 0.006(\text{syst.})$. [31] [32]

The Double Chooz experiment measures reactor antineutrino disappearance. Far detector is located at an average distance of 1050 m from the two reactor cores at the Chooz nuclear power plant. Measured: $\sin^2 2\theta_{13} = 0.090_{-0.029}^{+0.032}$. [33]

The Main Injector Neutrino Oscillation Search (MINOS) experiment was designed to measure the flavour composition of a muon neutrino beam at two locations using a near

and far detector located 1 km and 735 km from the target respectively. In 2006 the first muon neutrino disappearance results observed 215 events compared to an expectation of 336 ± 14 events and were consistent with disappearance via oscillations. [34] Most recently, in 2015 a joint analysis of accelerator and atmospheric neutrinos combining muon neutrino disappearance, electron neutrino appearance further improved the precision of parameter measurements with the results $|\Delta m_{32}^2| = |2.28 - 2.46| \times 10^{-3} \text{ eV}^2$ [35]

2.0.2 The Weak Force

Neutrinos interact with matter through the weak force in one of three flavour eigenstates (electron, muon or tau). The weak force is mediated by the electrically charged W^\pm and electrically neutral Z bosons.

Include feynam diagrams of the neutrino interactions.

A neutrino interacting with matter through the W boson will produce a charged lepton corresponding to the weak flavour of the incoming neutrino. This process can happen in reverse, with a charged lepton producing a neutrino with the same flavour and a W boson. Such processes involving a W boson are known as charged current interactions (CC interactions).

2.1 Neutrino Eigenstates

As current understanding has it, neutrinos come in three eigenstates of the weak force (electron, muon and tau) and three mass eigenstates (m_1 , m_2 or m_3).

Neutrinos interact with matter through the weak force in eigenstates of lepton flavour (ν_e , ν_μ and ν_τ). They propagate through vacuum in eigenstates of mass (ν_1 , ν_2 and ν_3). The eigenstates of mass and flavour are not equivalent, instead the flavour states are a superposition of the mass states. A neutrino of definite weak flavour α can be written as a linear combination of the mass states as follows,

$$|\nu_\alpha\rangle = \sum_{i=1}^3 U_{\alpha i}^* |\nu_i\rangle, \quad (2.1)$$

where $U_{\alpha i}^*$ is the element of the unitary PMNS (Pontecorvo, Maki, Nakagawa, and Sakata) matrix describing the coupling strength between the mass state i and the flavour state α .

The standard parametrisation of the PMNS matrix is in terms of a phase δ and three mixing angles, θ_{12} , θ_{13} and θ_{23} . The PMNS matrix is conventionally written as:

$$U = \begin{pmatrix} U_{e1} & U_{e2} & U_{e3} \\ U_{\mu1} & U_{\mu2} & U_{\mu3} \\ U_{\tau1} & U_{\tau2} & U_{\tau3} \end{pmatrix} \quad (2.2)$$

$$= \begin{pmatrix} c_{13}c_{12} & c_{13}s_{12} & s_{13}e^{-i\delta} \\ -c_{23}s_{12} - s_{13}s_{23}c_{12}e^{i\delta} & c_{23}c_{12} - s_{13}s_{23}s_{12}e^{i\delta} & c_{13}s_{23} \\ s_{23}s_{12} - s_{13}c_{23}c_{12}e^{i\delta} & -s_{23}c_{12} - s_{13}c_{23}s_{12}e^{i\delta} & c_{13}c_{23} \end{pmatrix} \quad (2.3)$$

$$= \begin{pmatrix} 1 & 0 & 0 \\ 0 & c_{23} & s_{23} \\ 0 & -s_{23} & c_{23} \end{pmatrix} \begin{pmatrix} c_{13} & 0 & s_{13}e^{-i\delta} \\ 0 & 1 & 0 \\ -s_{13}e^{i\delta} & 0 & c_{13} \end{pmatrix} \begin{pmatrix} c_{12} & s_{12} & 0 \\ -s_{12} & c_{12} & 0 \\ 0 & 0 & 1 \end{pmatrix} \quad (2.4)$$

where $s_{ij} \equiv \sin \theta_{ij}$, $c_{ij} \equiv \cos \theta_{ij}$ and δ is the CP violating phase. A non-zero value of δ would indicate charge-parity violation.

2.2 Neutrino Oscillation Probability in Vacuum

The following derivation of the neutrino oscillation probability follows [20] and [36].

A neutrino is produced via a weak interaction as a flavour eigenstate. At time $t = 0$ the flavour state, α , can be written as $|\nu_\alpha(t=0)\rangle$ and is the sum of the mass states $|\nu_i\rangle$:

$$|\nu_\alpha(t=0)\rangle = \sum_{i=1}^3 U_{\alpha i}^* |\nu_i\rangle. \quad (2.5)$$

As the neutrino propagates the mass states evolve. At time t we have:

$$|\nu_\alpha(t)\rangle = \sum_{i=1}^3 U_{\alpha i}^* e^{-ip_i \cdot x} |\nu_i\rangle, \quad (2.6)$$

where p_i is the four-momentum and x the four-position of mass state ν_i .

At time t the neutrino weakly interacts with matter in flavour state β :

$$\begin{aligned} \langle \nu_\beta | \nu_\alpha \rangle &= \sum_{j=1}^3 \sum_{i=1}^3 U_{\beta j} U_{\alpha i}^* e^{-ip_i \cdot x} \langle \nu_j | \nu_i \rangle \\ &= \sum_{j=1}^3 U_{\beta j} U_{\alpha j}^* e^{-ip_j \cdot x}. \end{aligned} \quad (2.7)$$

Assuming all mass states have the same three-momentum \mathbf{p} ,

$$\begin{aligned}
p_j \cdot x &= E_j t - \mathbf{p} \cdot \mathbf{x} \\
&= t \sqrt{|\mathbf{p}|^2 + m_j^2} - \mathbf{p} \cdot \mathbf{x}
\end{aligned} \tag{2.8}$$

Since neutrinos are extremely light ($m_\nu < 2 \text{ eV}$ [20]) and, in the case of accelerator experiments, travel at close to the speed of light we can make the approximations, $m_j \ll E_j$, $t = L$ and $\mathbf{p} \cdot \mathbf{x} = |\mathbf{p}|L$. Using a binomial expansion we find,

$$p_j \cdot x = |\mathbf{p}|L \left(1 + \frac{m_j^2}{2|\mathbf{p}|^2} \right) - |\mathbf{p}|L = \frac{m_j L}{2E} \tag{2.9}$$

Combining Equations 2.7 and 2.9 we get $\langle \nu_\beta | \nu_\alpha \rangle = \sum_{j=1}^3 U_{\beta j} U_{\alpha j}^* e^{-i \frac{m_j L}{2E}}$.

The probability of observing the neutrino in flavour state β after travelling distance L and given initial flavour state α is given by:

$$\begin{aligned}
P_{\alpha \rightarrow \beta} &= |\langle \nu_\beta(t) | \nu_\alpha(t) \rangle|^2 \\
&= \left(\sum_{j=1}^3 U_{\beta j} U_{\alpha j}^* e^{-i \frac{m_j L}{2E}} \right) \left(\sum_{i=1}^3 U_{\beta i}^* U_{\alpha i} e^{i \frac{m_i L}{2E}} \right).
\end{aligned} \tag{2.10}$$

Finally, we find:

$$\begin{aligned}
P_{\alpha \rightarrow \beta} &= \delta_{\alpha\beta} - 4 \sum_{i>j} \Re[U_{\alpha i}^* U_{\alpha j} U_{\beta i} U_{\beta j}^*] \sin^2 \left(\frac{\Delta m_{ij}^2}{4E} L \right) \\
&\quad + 2 \sum_{i>j} \Im[U_{\alpha i}^* U_{\alpha j} U_{\beta i} U_{\beta j}^*] \sin^2 \left(\frac{\Delta m_{ij}^2}{2E} L \right),
\end{aligned} \tag{2.11}$$

where $\Delta m_{ij}^2 \equiv m_i^2 - m_j^2$ and $\delta_{\alpha\beta}$ is the Kronecker delta. The equation shows that the neutrino oscillation probability depends on the parameters of the PMNS matrix and the value of the two sinusoidal arguments. The probability depends on the mass splittings Δm_{12}^2 , Δm_{13}^2 , Δm_{23}^2 , and alters with the length of the baseline, L , and the energy of the neutrino beam, E .

2.3 Neutrino Oscillation Parameter Measurements

The experimentally measured values of the neutrino oscillation parameters are given in Table 2.1. The measurements of the oscillation parameters have been made using reactor, solar, accelerator and atmospheric neutrino experiments.

Parameter	Average of measurements
$\sin^2 \theta_{12}$	0.304 ± 0.014
$\Delta m_{21}^2 [10^{-5} \text{ eV}^2]$	7.53 ± 0.18
$\sin^2 \theta_{23}$	0.51 ± 0.05 (0.50 ± 0.05)
$\Delta m_{32}^2 [10^{-3} \text{ eV}^2]$	2.44 ± 0.06 (-2.51 ± 0.06)
$\sin^2 \theta_{13} [10^{-2}]$	2.19 ± 0.12

Table 2.1: The average value of measurements and 1σ error of the neutrino oscillation parameters from [20]. Measurements that differ under the assumption of inverted ordering (rather than normal ordering) are provided within parenthesis.

The two mass differences and three mixing angles have all been measured. The sign of the mass difference has been determined for Δm_{12}^2 (ν_1 is less massive than ν_2) but not for Δm_{23}^2 . This means that it is not known whether ν_3 is more or less massive than the two other mass states, the former and later cases are known as Normal Ordering or Inverted Ordering respectively. A schematic showing the Normal and Inverted Ordering is shown in Figure

Tentative measurements of the CP violating phase δ_{CP} have been made [37] but the value remains relatively unknown.

Current measurements suggest that $\sin^2 \theta_{23} = 0.5$ which would mean $\cos^2 \theta_{23} = 0.5$. In this case, $U_{\mu 2} = U_{\tau 3} = \frac{1}{2}c_{13}$ (see Equation 2.4). These two PMNS matrix elements define the mixing of ν_μ and ν_τ with ν_3 . Therefore, if $\sin^2 \theta_{23} = 0.5$ then the third mass state is composed of equal parts ν_μ and ν_τ , this is known as maximal mixing. If nature has chosen non-maximal mixing then discovering the octant (whether $\sin^2 \theta_{23}$ is less or more than 0.5) will determine whether the third mass state is composed of more ν_μ or more ν_τ .

2.4 Two-Flavour Approximation

In many experimental cases the neutrino oscillation probability can be approximated as the result of two-flavour mixing. This two flavour oscillation probability and the necessary approximation will be outlined in this section.

For long baseline neutrino oscillation experiments it is useful to write the phase $\frac{\Delta m_{ij}^2}{4E}L$ in units of the same scale as the experiment. This is done using units of eV^2 for Δm_i^2 , GeV for E and km for L . Restoring factors of \hbar and c and applying the appropriate unit

conversions we find:

$$\frac{\Delta m_{ij}^2 c^3}{4E\hbar} L \approx 1.27 \frac{\Delta m_{ij}^2 [\text{eV}^2]}{E [\text{GeV}]} L [\text{km}]. \quad (2.12)$$

Let us use the oscillation channel relevant to this thesis as the example. In the three flavour case (Equation 2.11), the muon neutrino survival probability is:

$$P_{\mu \rightarrow \mu} = 1 - 4 \sum_{i>j} |U_{\mu i}|^2 |U_{\mu j}|^2 \sin^2 \left(\frac{\Delta m_{ij}^2}{4E} L \right), \quad (2.13)$$

where the imaginary component of Equation 2.11 is zero because in this case $\Im[U_{\mu i}^* U_{\mu i}] = 0$.

The elements of the PMNS matrix, $U_{\mu i}$, can be simplified considering the current measured values. Table 2.1 shows that the value of $\sin^2 \theta_{13}$ is very small relative to the two other mixing parameters. Using the approximations $\sin \theta_{13} \approx 0$ and $\cos \theta_{13} \approx 1$ the relevant PMNS elements (see Equation 2.4) can be approximated as:

$$\begin{aligned} |U_{\mu 1}|^2 &\approx s_{12}^2 c_{23}^2 \\ |U_{\mu 2}|^2 &\approx c_{12}^2 c_{23}^2 \\ |U_{\mu 3}|^2 &\approx s_{23}^2 \end{aligned} \quad (2.14)$$

Experimental results have shown that the mass splitting Δm_{12}^2 is very small relative to Δm_{13}^2 and Δm_{23}^2 (see Table 2.1) [20], which allows the approximation: $\Delta m_{13}^2 \simeq \Delta m_{23}^2$. For long baseline neutrino oscillation experiments the oscillations associated with the atmospheric and solar mass splittings can be approximated to be de-coupled. This is because the atmospheric mass splitting is ~ 30 times larger than the solar mass splitting. As an example, let us take the NOvA experiment with $L = 810$ km and $E \sim 2$ GeV. For the NOvA experiment we have:

$$\sin^2 \left(\frac{1.27 \Delta m_{12}^2}{E} L \right) = \sin^2 \left(\frac{1.27 \times 7.53 \times 10^{-5}}{2} \times 810 \right) \approx \sin^2 0.04 \approx 0. \quad (2.15)$$

With the above simplifications, the muon neutrino survival probability can be expressed as:

$$\begin{aligned} P_{\mu \rightarrow \mu} &\simeq 1 - 4s_{23}^2 c_{23}^2 (s_{12}^2 + c_{12}^2) \sin^2 \left(\frac{1.27 \Delta m_{atm.}^2}{E} L \right) \\ &\simeq 1 - \sin^2 2\theta_{23} \sin^2 \left(\frac{1.27 \Delta m_{atm.}^2}{E} L \right), \end{aligned} \quad (2.16)$$

where $\Delta m_{atm.}^2 \equiv \Delta m_{32}^2 \simeq \Delta m_{13}^2$. From this equation it can be seen that the disappearance probability has an oscillatory form. The overall magnitude of the oscillation is governed by $\sin^2 2\theta_{23}$ and the period of the oscillation is defined by $\frac{\Delta m_{atm.}^2 L}{E}$.

2.5 Matter Effects

Neutrinos propagating through matter experience the weak force through NC interactions and coherent forward scattering. Ordinary matter is composed, in part, of electrons but not muons or taus. For this reason coherent forward scattering (shown in Figure 2.1) is only experienced by electron neutrinos. In addition, NC interactions with matter are flavour independent and so do not affect neutrino oscillations. This additional scattering amplitude causes oscillations involving ν_e or $\bar{\nu}_e$ to have different probabilities relative to oscillation in vacuum.

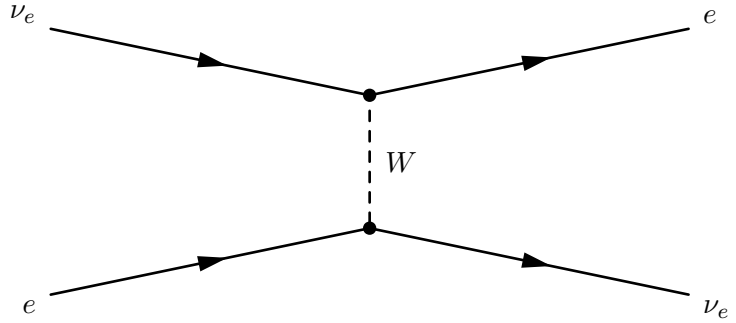


Figure 2.1: Feynman diagram of coherent forward scattering of ν_e on e .

The evolution of the neutrino flavour states is given by

$$i \frac{d}{dx} \begin{pmatrix} \nu_e \\ \nu_\mu \\ \nu_\tau \end{pmatrix} = H \begin{pmatrix} \nu_e \\ \nu_\mu \\ \nu_\tau \end{pmatrix}, \quad (2.17)$$

where H is the Hamiltonian. In matter H is given by

$$H = U \begin{pmatrix} \frac{m_1^2}{2E} & 0 & 0 \\ 0 & \frac{m_2^2}{2E} & 0 \\ 0 & 0 & \frac{m_3^2}{2E} \end{pmatrix} U^\dagger + \begin{pmatrix} \sqrt{2}G_F N_e & 0 & 0 \\ 0 & 0 & 0 \\ 0 & 0 & 0 \end{pmatrix}, \quad (2.18)$$

where G_F is the Fermi constant and N_e is the electron number density of the medium.

Matter effects modify the terms $\sin(\Delta_{31})$ and $\sin(\Delta_{21})$ (where $\Delta_{ij} \equiv \frac{\Delta m_{ij}^2}{4E} L$) in Equation 2.11 by substituting:

$$\sin(\Delta_{ij}) \rightarrow \frac{\Delta_{ij}}{\Delta_{ij} \mp aL} \sin(\Delta_{ij} \mp aL), \quad (2.19)$$

where $a = \frac{G_F \rho_e}{\sqrt{2}}$, the top sign refers to neutrinos and the bottom sign to antineutrinos.

[38]

For the Normal Ordering, matter effects enhance the appearance probability $\nu_\mu \rightarrow \nu_e$ but suppress the appearance probability $\bar{\nu}_\mu \rightarrow \bar{\nu}_e$. Conversely, for the Inverted Ordering matter effects suppress the ν_e appearance probability and enhance the $\bar{\nu}_e$ probability.

Matter effects have the opposite consequence for neutrinos and antineutrinos and so can be confused with the effect of true CP violation. Figure 2.2 illustrates the ambiguity between CP and matter effects when measuring the neutrino and antineutrino appearance. The figure shows regions of bi-probability where it is possible to disentangle the contributions of matter effects and CP violation. In particular, for the inverted hierarchy and $\delta_{CP} = 3\pi/2$ (the starred point) NOvA would be able to measure the mass ordering to be Normal with some confidence. This point would correspond to measured probabilities of $P(\bar{\nu}_e) = 0.025$ and $P(\nu_e) = 0.06$. Conversely, if NOvA measures $P(\bar{\nu}_e) = 0.04$ and $P(\nu_e) = 0.04$ then it will not be possible to distinguish between two possible scenarios: either the ordering is normal and $\delta_{CP} \approx \pi/2$ or the ordering is inverted and $\delta_{CP} \approx 3\pi/2$. The two ellipses shown are for fixed values of $\sin^2(2\theta_{13})$, $\sin^2(2\theta_{23})$ and Δm_{32}^2 . The effect of increasing (decreasing) θ_{23} is to increase (decrease) both appearance probabilities and make the ellipses less (more) ambiguous.

2.6 Latest Results

About 5 pages

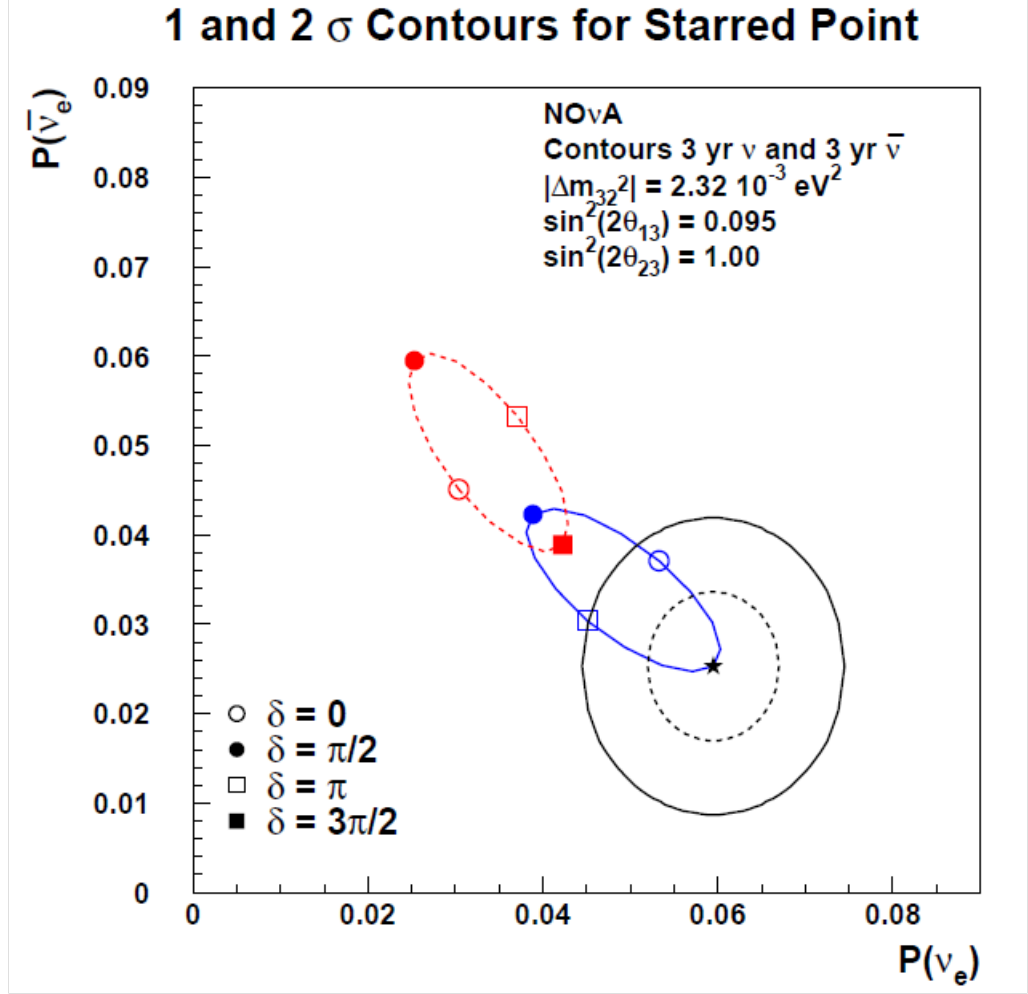


Figure 2.2: Bi-probability plot of ν_e appearance for the NOvA experiment. The solid blue and dotted red ellipses show the possible probability measurements for the Normal and Inverted Ordering respectively. The effect of altering δ_{CP} is to trace out the ellipse. Selected values of δ_{CP} are shown by the square and circle markers.

Chapter 3

The NOvA Experiment

The NuMI Off-axis ν_e Appearance (NOvA) experiment is designed to make precise measurements of muon neutrino disappearance and electron neutrino appearance in a muon neutrino beam. The experiment consists of two functionally equivalent detectors which measure the neutrino energy and flavour composition of the Neutrinos at the Main Injector (NuMI) beam. The detectors are constructed from PVC tubes filled with liquid scintillator and are highly granular to distinguish neutrino induced signals and background. The 300 ton near detector is located on site at Fermilab 1.015 km from the NuMI target. The 14 kiloton far detector is located at a site near Ash River, Minnesota and is 810 km from the NuMI target. The baseline and mean neutrino energy are chosen such that the far detector sees the first oscillation maximum driven by $\Delta m_{32}^2 \text{ eV}^2$. Both detectors are placed off-axis from the centre of the NuMI beam to enhance the sensitivity to electron neutrino appearance and muon neutrino disappearance.

The original design of the NOvA experiment is laid out in the technical design report (TDR) [38] and the constructed experiment design differs only slightly. The details of the constructed experiment, including the neutrino beam source and the two detectors, are discussed in the following chapter.

3.1 The NuMI Beam

The NOvA experiment's neutrino source is the Neutrinos at the Main Injector (NuMI) beam at Fermilab. The following section briefly describes the process by which the NuMI beam is created. More details are available in Ref [39].

The NuMI beam-line extracts batches of approximately 4.8×10^{13} 120 GeV protons from the Main injector and directs them onto a 0.95 m long graphite target. Each extrac-

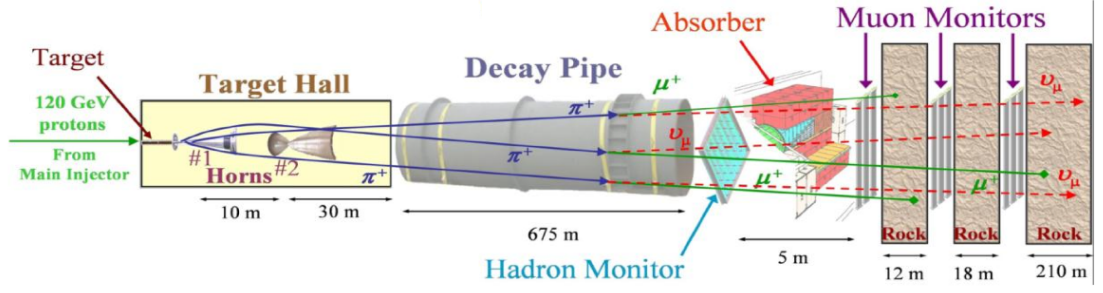


Figure 3.1: A diagram showing the layout of the NuMI beam. [39]

tion of protons is known as a beam spill. There is typically an interval of 1.33 s between beam spills.

An instructive diagram of the NuMI beam facility is presented in Figure 3.1. The Figure shows the beam components including the Target Hall, Decay Pipe, Hadron Monitor, Absorber and Muon Monitors. Within the target hall, collisions between the accelerated protons and the carbon atoms of the target produce a plethora of secondary particles (mostly pions and kaons). The charged mesons of one sign (or the other) are focused into a beam by two magnetic focussing horns. The resulting beam of charged mesons then enters a 675 m long He filled decay pipe. Along this length the mesons decay predominantly to charged leptons and neutrinos. The decay pipe is followed by a hadron monitor, an absorber, muon monitors and about 240 m of rock. The remaining muons are absorbed by the rock leaving a beam of neutrinos. After the rock the beam arrives at the NOvA near detector before continuing through the Earth's crust for 810 km where it reaches the NOvA far detector.

3.1.1 Focussing Horns

Two magnetic horns are used to focus the mesons created by collisions of protons with the NuMI target into a beam. Figure 3.2 shows the NuMI target, Horn 1, Horn 2 and example meson trajectories. The design of the focussing horns allows three potential Horn 1 to Horn 2 separations corresponding to low, medium and high energy beam. In the medium energy tune the Target is placed 1.3 m upstream from the opening of Horn 1 while Horn 2 is placed 23 m downstream relative to the front face of Horn 1. The NuMI horns are setup in aforementioned medium energy configuration for the NOvA era.

The horns act as a lens where the focal length is proportional to the momentum of the mesons. Changing the current direction within the focussing horns, choosing either forward or reverse horn current, changes the direction of the magnetic field and therefore

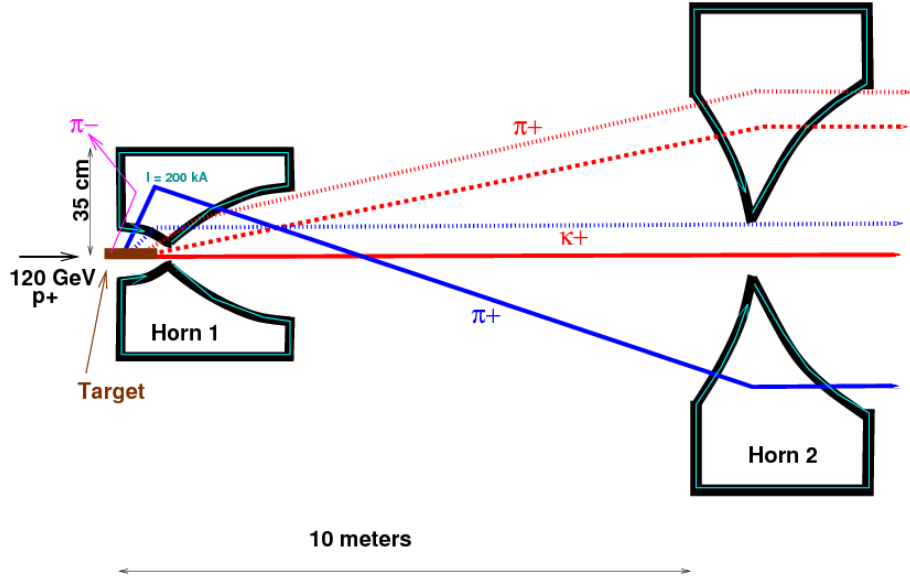


Figure 3.2: A diagram of the magnetic focussing horns operating in forward horn current mode. Positively charged mesons arriving from different directions are focussed by the combination of the two horns. The trajectory of positively charged mesons that are over or under focussed by Horn 1 can be corrected by Horn 2. [39]

the sign of the mesons that are focussed. Operating the horns with forward or reverse horn current selects positively or negatively charged mesons respectively, leading to a predominantly neutrino or antineutrino beam respectively.

3.1.2 Off-axis Experiment Design

The NOvA detectors are both placed 14 mrad off the axis of the NuMI beam. The dominant decay process used to produce a neutrino beam is a two-body decay, where a pion (or kaon) decays to a neutrino and a muon. The two body decay occurs isotropically in the parent particle's rest frame. In the lab frame the parent particle is not at rest when decaying, for pion and kaon decay this boosts the neutrinos in the direction of the parent particle. For small angles, the flux per decay (Φ) and energy (E_ν) of neutrinos produced by pion decay ($\pi \rightarrow \nu_\mu + \mu$) are given by

$$\Phi = \left(\frac{2\gamma}{1 + \gamma^2\theta^2} \right)^2 \frac{A}{4\pi z^2}, \quad (3.1)$$

$$E_\nu = \frac{0.43E_\pi}{1 + \gamma^2\theta^2}, \quad (3.2)$$

where E_π is the energy of the parent pion, m_π the mass of the parent pion, $\gamma = E_\pi/m_\pi$, θ the angle between the parent pion and outgoing neutrino directions, A is the cross-sectional

area and z is the distance from the pion decay vertex.

Equations 3.1 and 3.2 are shown as functions of pion energy for the Medium Energy NuMI Tune in Figure 3.3. The Figure also shows the effect of four off-axis angles ($\theta = 21$ mrad, $\theta = 14$ mrad, $\theta = 7$ mrad and $\theta = 0$ mrad).

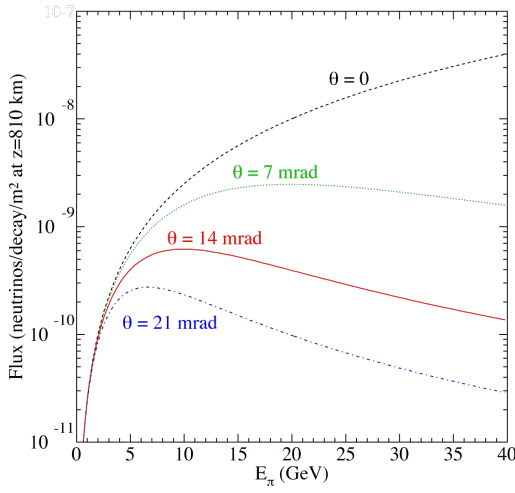
Figure 3.4 shows the number of neutrino events as a function of the charged current ν_μ energy for the Low (Figure 3.4a) and Medium (Figure 3.4b) Energy Tune for various off-axis angles. The plot shows that as the off-axis angle is increased the mean and width of the energy distribution decreases.

For the Medium Energy Tune, figure 3.3b shows that at 14 mrad the neutrino energy does not have a strong dependence on the parent pion energy. In addition, figure 3.4b shows that at 14 mrad the Medium Energy Tune produces a narrow energy neutrino beam with approximately 4 times more neutrinos at 2 GeV than the on-axis scenario. This peak at 2 GeV is well matched to the expected energy of the first oscillation maximum which is expected to occur at 1.6 GeV for NOvA's L/E (experiment baseline to mean neutrino energy ratio) and for $\Delta m_{32}^2 = 2.4 \text{ meV}^2$.

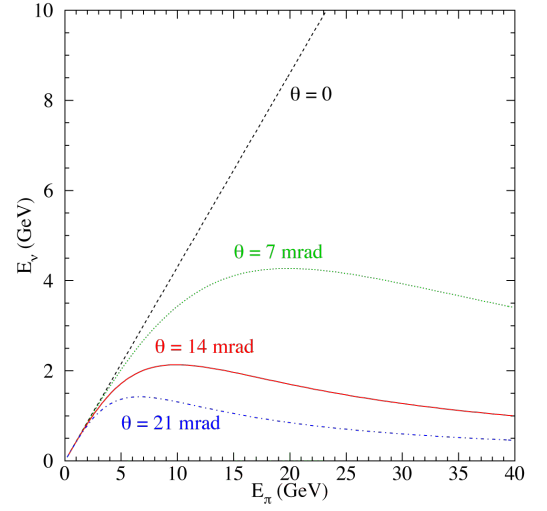
As described above, placing the detector off-axis increases the flux at the expected oscillation maximum. In addition, the narrow energy range of the off-axis beam reduces background events. Neutral current events are an important background source whose topologies can be hard to distinguish from electron showers produced by ν_e charged current events. For neutral current events, the neutrino carries a significant amount of the energy away and the energy visible within the detector tends to “feed down” to lower energies. For a narrow band off-axis beam, this feed down tends to shift the neutral current events towards lower energies outside the ν_e appearance signal energy window. Figure 3.5 shows the number of ν_μ , ν_e and neutral current events as a function of visible energy. The bulk of the neutral current events (black histogram) are shown to shift below the signal region (red-hatched histogram).

3.2 The NOvA Detectors

The NOvA collaboration performs measurements of both ν_μ disappearance and ν_e appearance and the NOvA detectors are designed to be able to identify the muons and electrons produced in charged-current neutrino interactions. The ν_e appearance analysis has the potential to be overrun with neutral current background events, as a large potential background comes from π^0 s produced in neutral current events which can fake an electron shower. The NOvA detectors are constructed from low Z materials (primarily car-

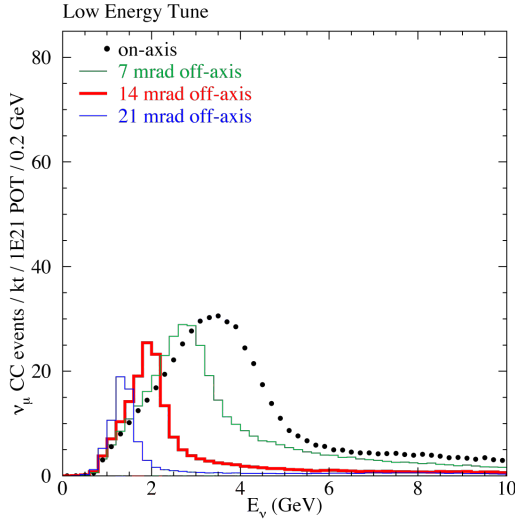


(a) Neutrino flux vs. pion energy.

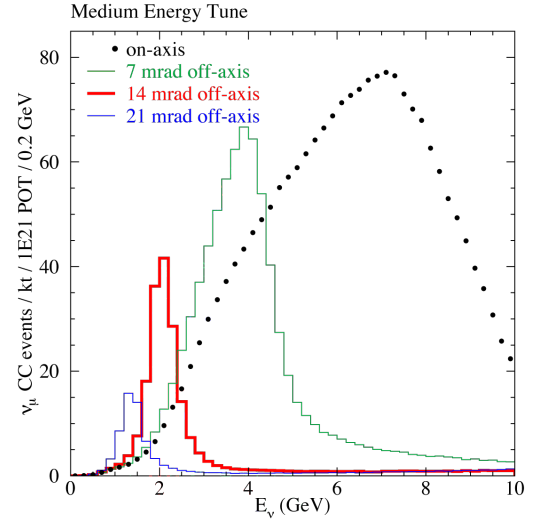


(b) Neutrino vs. pion energy.

Figure 3.3: The above distributions are for the medium energy tune NuMI beam as viewed from a site located 800km from the NuMI target and off-axis by an angle θ . The left plot shows the neutrino flux as a function of the energy of the parent pion for different off-axis angles. The right plot shows the neutrino energy as a function of the parent pion energy for different off-axis angles. [38]



(a) Low Energy Tune neutrino energy.



(b) Medium Energy Tune neutrino energy.

Figure 3.4: Charged current ν_μ event rates vs. neutrino energy in the absence of oscillations. The distributions are found for a detector which is 800 km from the NuMI target and for various off-axis angles. [38]

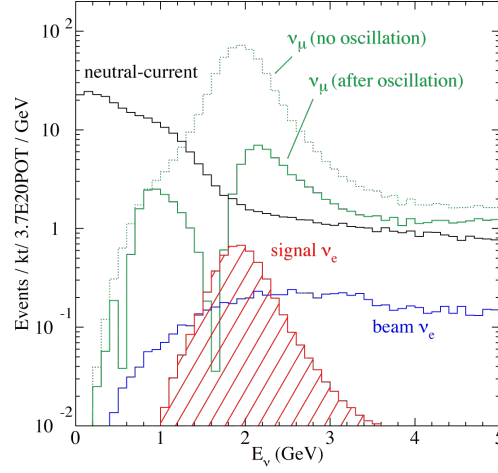


Figure 3.5: Simulated visible energy distributions for ν_μ charged current events with and without oscillations, ν_e oscillation signal events, intrinsic beam ν_e events and neutral current events. The simulation assumes an off-axis position of 12 km at 810 km, $\Delta m^2 = 2.5 \times 10^{-3} \text{eV}^2$, $\sin^2(2\theta_{23}) = 1.0$ and $\sin^2(2\theta_{13}) = 0.1$. [38]

bon) to aid in the distinction between neutrino interaction signatures and the potentially troublesome background events. The constructed detectors have a Moliere radius [20] of approximately 11 cm which is equivalent to the depth (width) of two (three) NOvA cells.

A diagram of the two detectors is shown in Figure 3.6. The near and far NOvA detectors are almost functionally identical. Besides the different masses, there are a few physical differences designed considering the proximity to the NuMI beam and the depth of the detector relative to ground level. The smaller near detector has a so called “muon catcher” and has a higher rate of readout. Whilst the far detector is constructed with an overburden to mitigate the cosmic ray background. The construction common among both detectors will be discussed in the following sub-sections. The details specific to the far and near detectors will be discussed in sub-sections 3.2.7 and 3.2.8 respectively.

3.2.1 The Basic NOvA Detector Element

The basic unit of the NOvA detectors is a rectangular rigid PVC (Polyvinyl chloride) cell which contains liquid scintillator and a wavelength-shifting fibre. Figure 3.8 shows the NOvA cell, looped wavelength-shifting fibre and an example charged particle. The wavelength-shifting fibre, which is twice the length of the cell, is looped at the bottom of the cell such that the captured light travels in two directions to the instrumented top end of the cell. Each end of the looped fibre is directed onto one pixel of an Avalanche Photo Diode (APD) array. The APD converts the light from the fibre into a digital signal.

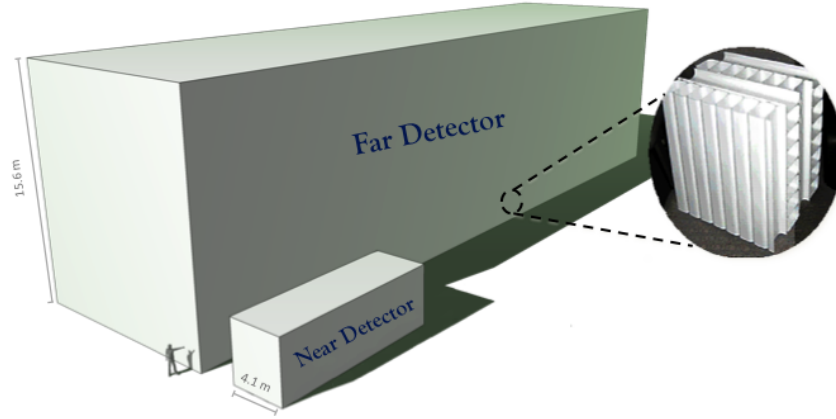


Figure 3.6: Scaled depiction of the near and far NOvA detectors with respect to the average person. The alternating alignment of the NOvA cells is shown by the inset.

The NOvA cells are made from highly reflective titanium dioxide loaded rigid PVC. The cells have 2 to 4.5 mm thick walls, an interior depth of 5.9 cm along the beam direction and an interior width of 3.8 cm transverse to the beam direction. The thickness of the cell walls varies due to structural considerations. The length of the cells differs between the two detectors, the far detector cells have a length of 15.5 m whilst the near detector cells are 3.6 m long.

3.2.2 Liquid Scintillator

Approximately 65% of the NOvA detector mass is composed of the liquid scintillator held within the cells. The composition of the liquid scintillator is shown in Table 3.1, which shows that the scintillator is composed mainly of mineral oil along with 5.23% pseudocumene as the scintillant. The scintillant emits scintillation light with a spectrum peaked between 360 - 390 nm. Wavelength shifting chemical additives PPE and bis.MSB are added to shift the initial light spectrum to 400 - 450 nm to match the absorption spectra of the wavelength-shifting fibre.

3.2.3 Wavelength Shifting Fibre

The wavelength-shifting fibre has a diameter of 0.7 mm and a core of polystyrene mixed with R27 dye (as the wavelength shifter) at a concentration of 300 ppm. The fibre has two coatings (contributing about 3% of the fibre diameter) of materials with a lower refractive index than the core which facilitates total internal reflection within the fibre. The fibre is first coated with a thin acrylic layer of PMMA and second with fluor-acrylic.

Component	Purpose	Mass fraction %
mineral oil	solvent	94.63
pseudocumene	scintillant	5.23
PPO	waveshifter	0.14
bis-MSB	waveshifter	0.0016
stadis-425	anti-static agent	0.0010
tocopherol	antioxidant	0.0010

Table 3.1: Chemical composition of the NOvA liquid scintillator. [40]

The 400 - 450 nm light emitted by the liquid scintillator is absorbed by the fibre and then wavelength shifted to 490 - 550 nm. As light travels down the fibre it is attenuated, by a factor of about 10 in the far detector, with light in the range 520 - 550 nm preferentially surviving.

3.2.4 Avalanche Photo Diode

The light exiting the fibre ends is detected by an Avalanche Photodiode (APD) and converted into an electronic signal pulse. Figure 3.7 shows a photograph of a NOvA APD and the array of 32 pixels. Each pixel is interfaced with both ends of a single wavelength-shifting fibre. Each APD is connected to a front end board that prepares the signals from the APD for the data acquisition system.

The NOvA APD was chosen because it has an 85% quantum efficiency for the 520 - 550 nm light exiting the fibre ends. The thermal noise generated by each APD is reduced by thermo-electric coolers which cool the APDs to -15°C.

3.2.5 Data Acquisition System

NOvA's data acquisition system continuously reads out all the information from the APDs. The information is temporarily stored in a buffer farm and awaits a decision as to whether it should be permanently recorded or rejected. The decision can be made by either online triggering algorithms or by receiving a trigger signal from an external source. The NuMI beam spill signal is an example of an external source trigger.

Each APD is continuously readout by an front end board, which handles the pedestal subtraction and pulse shaping for each signal from the APD. The pedestals are determined for each APD pixel by measuring the baseline noise level. The signal pulses are shaped with a characteristic rise and fall time. When a signal is triggered the signal sample is read

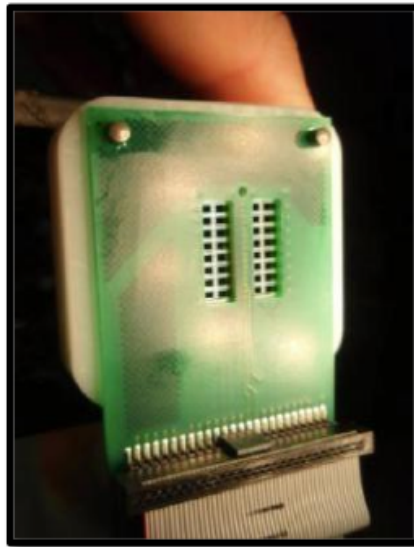


Figure 3.7: The NOvA APD containing an array of 32 pixels.

out along with the three immediately preceding samples in a process called “multi-point readout”. Once the data is permanently recorded, the known pulse shaping parameters are used to fit the four samples and provide more precise timing resolution.

The front end board transmits the digitised data to a data concentrator module, which can take inputs from up to 64 front end boards. Each data concentrator module collects all the information from the connected front end boards during a $50 \mu s$ window (“microslice”). This data packet is then sent to and stored in the buffer farm until online trigger processes decide whether to record or reject the data.

3.2.6 Detector Assembly

The NOvA detectors are constructed from the cells described in Section 3.2.1. 16 cells are extruded together in one unit to form an extrusion. Figure 3.9 shows the end-on view of an extrusion with a width of 63.5 cm and depth of 6.6 cm. Two extrusions are placed side by side to form an extrusion module consisting of 32 cells. Figure 3.10 shows an extrusion module consisting of 32 cells, end plate, side seal, manifold cover, snout and electronics box. The module ends are capped by the end plate so that the modules can contain the liquid scintillator. The other end is capped by a manifold cover which contains the liquid scintillator in the horizontal cells and directs the 32 fibre end pairs to the 32 APD pixels in the NOvA APD.

Flat planes of cells are constructed from multiple modules glued together side by side. Figure 3.11 shows a cross-section of multiple plane layers and the alternating orthogonal

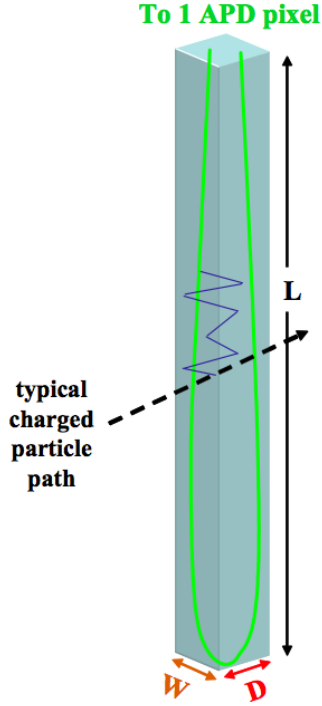


Figure 3.8: A NOvA cell consisting of an extruded PVC tube filled with liquid scintillator and a looped wavelength-shifting fibre.



Figure 3.9: An end on view of an extrusion constructed from 16 NOvA cells.

cell orientation. The planes are layered with alternating orthogonal orientations, such that the orientation of the cells making up the plain alternate between horizontal and vertical from plane to plane. The orthogonal orientation of the planes allows for three dimensional reconstruction of tracks passing through multiple planes. Planes are glued together in the orthogonal arrangement described above to form one solid detector piece called a block, consisting of 32 or 24 planes in the far detector or near detector respectively.

3.2.7 The Far Detector

The 14 kiloton far detector is located 810 km from the NuMI target, approximately 10 m below ground level and at an elevation of 372 m above sea-level. The neutrino beam enters the detector travelling at an angle of 3° upwards. The detector is constructed, as described in Section 3.2.6, from 344,064 15.5 m long cells which form 896 planes normal to the beam direction. The detector mass is approximately 65% liquid scintillator and 35% PVC.

As described above, the far detector is built on the surface above sea level so cosmic rays will be a major source of background events. The background due to cosmic rays is

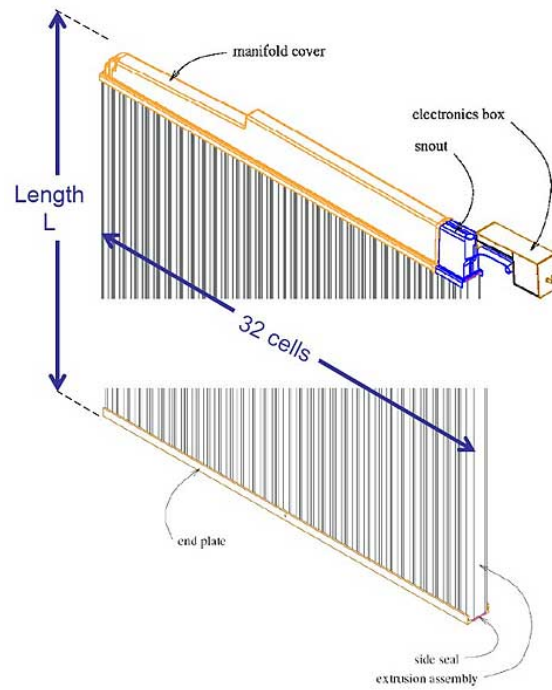


Figure 3.10: A side on view of an extrusion module constructed from two extrusions of 16 cells, an end plate, a side seal, a manifold cover, a snout and an electronics box

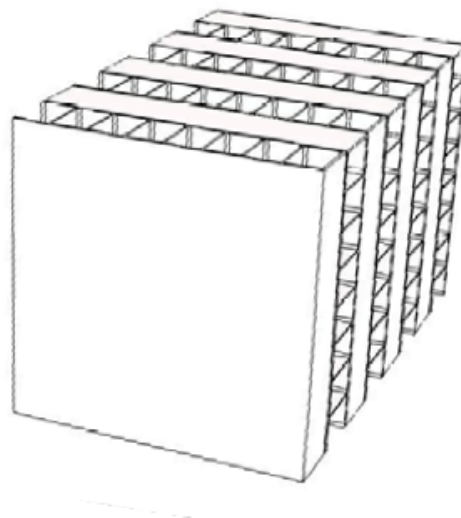


Figure 3.11: Cut out of the NOvA detector showing the alternating orientation of the cells within the stacked planes.

mitigated using selection cuts and a shielding overburden above the detector. For the ν_μ disappearance analysis the background is primarily due to cosmic ray muons which are almost entirely removed using cuts. For the ν_e appearance analysis, the background is primarily cosmic ray photons whose interactions within the detector can be mistaken for an electron shower. During a six year run the far detector without overburden shielding will see approximately 1600 background events due to cosmic ray photons. In order to reduce this background source to less than one event requires approximately 9 radiation lengths of material above the detector surface. Additional radiation lengths will then help to contain any showers caused by interactions within the overburden. With this in mind, the far detector building was constructed with a 122 cm thick concrete enclosure which supports a 15 cm thick overburden of barite. Together, the concrete enclosure and barite overburden provide 12 radiation lengths of shielding.

3.2.8 The Near Detector

The NOvA near detector is located on site at Fermilab next to the MINOS Hall. Figure 3.12 is a diagram of the MINOS Hall area showing the MINOS Shaft, NuMI beam-line, MINOS Hall, NuMI Beam-line, 14.6 mrad off-axis beam and the NOvA Near Detector cavern. The near detector is 105 m underground and 1.015 km from the NuMI target. The near detector therefore sees a higher flux of NuMI neutrino events and a lower flux of cosmic rays than the far detector. The neutrino beam enters the detector travelling downwards at an angle of 3° .

A diagram of the near detector is shown in Figure 3.13. The Figure shows the NOvA Near Detector cavern, access catwalks, and the fully active detector and muon catcher detector sections. The detector is constructed in a similar fashion to the far detector with 20,192 cells arranged in 214 planes, each plane is comprised of 3 modules (except in the muon catcher). The detector has a width and height (except in the muon catcher) of 4.2 m and a length of 15.8 m. The near detector is functionally equivalent to the far detector with the exception of two distinguishing features.

First, a muon catcher is placed at the downstream end of the near detector in order to help range out muons from few GeV charged current ν_μ interactions which would not otherwise stop within the detector. The muon catcher is constructed from layers of steel and liquid scintillator planes. The steel planes are 10 cm thick and are separated by two (one horizontal and one vertically aligned) scintillator planes. The vertical planes consist of three modules while the horizontal planes are made from just two modules. Therefore,

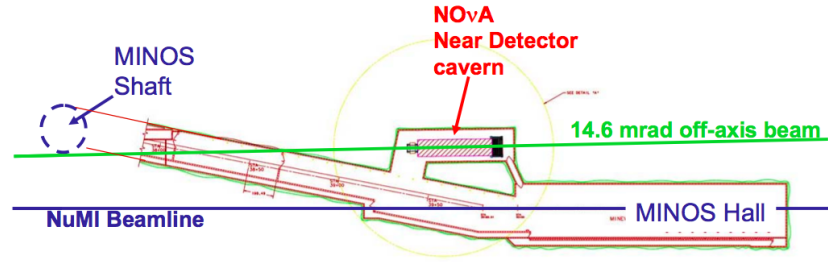


Figure 3.12: Bird's-eye view diagram of the NuMI Beam-line, MINOS Hall, MINOS shaft and the NOvA near detector cavern

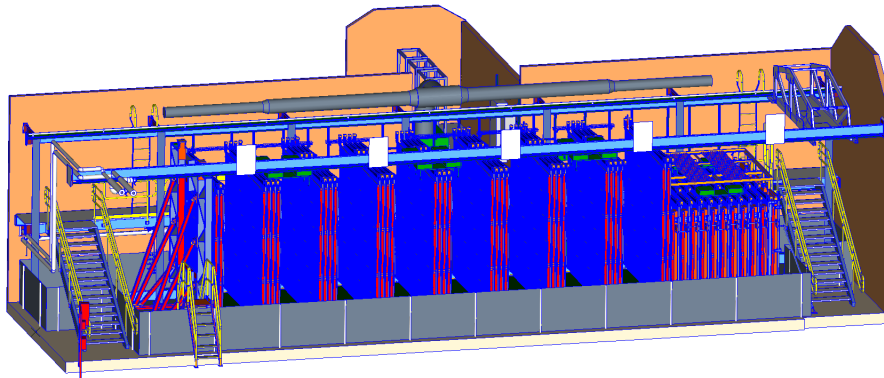


Figure 3.13: Technical drawing of the NOvA near detector and cavern. The NuMI beam enters from the left. The muon catcher planes are shown on the right hand side of the detector. Note that only some of the planes have been drawn to aid visualisation of the detector layout.

the sets of steel and scintillator planes are three modules wide (the same as the rest of the detector) but only two modules high. Ten of these steel and liquid scintillator plane sets are stacked to form the muon catcher. The downstream end of the muon catcher has an additional 3 liquid scintillator planes.

Second, the near detector electronics are setup to sample each channel (APD pixel) four times more frequently (every 125 ns) than in the far detector to help handle the data pileup. The near detector sees approximately 5-10 neutrino interactions per beam spill (10 μ s window) while the far detector sees approximately 60-70 cosmic rays per 550 μ s window spread out over approximately 17 times more channels. The faster sampling rate improves the timing resolution of hits in the detector. With better timing resolution, pileup events are more easily distinguished from one another.

3.3 Monte Carlo Simulation

The NOvA experiment is simulated using several Monte Carlo packages. The simulation involves several stages, each using information from the previous step. Simulations model the NuMI beam, subsequent neutrino interactions within the detectors, the propagation of particles through the detector geometry, and finally the modelling of the detector response to those particles.

The creation and propagation of the NuMI beam is simulated using FLUKA and Geant4 through the FLUGG interface [?, ?, ?]. The beam simulation produces files containing a flux of simulated neutrinos with given flavour, energy and direction. Details of each neutrino's parent are retained.

Chapter 4

NOvA Analysis Methodology

4.1 Extrapolation

4.2 Selection

4.3 Reconstruction

4.4 Calibration

4.5 GENIE Tune

4.6 Evaluation of Systematics

show effect of each systematic and shift in Norm, mean energy and rms of neutrino energy.

4.6.1 Calibration

xy systematic and y shift systematic

4.6.2 Birks

Birks B,C, ? Expand on rock muon issue

4.6.3 Noise

Chapter 5

Analysis Improvements

Three (x2, for dm and sin) metrics for each improvement: SA BF (max-mix rej.), MINOS (max-mix rej.), and T2K BF (limit and rej. of (2.5,0.4))

5.1 Hadronic Energy Fraction Binning

5.2 Optimising Neutrino Energy Binning

5.3 Hybrid Selection Using ReMId and CVN

5.4 All Analysis Improvements Combined

Then respin number of HadEFrac. bins again w/ energy bins and hybrid. Iterate until while improvements are shown.

5.5 Systematic Uncertainty

5.6 Energy Resolution Binning

Energy resolution binning was implemented in MINOS to improve the sensitivity of the experiment. Techniques similar to those found in [41] will be used in the following chapter to improve the sensitivity of the NOvA experiment.

Table 5.3 shows the shifts in the values of $\sin^2 2\theta_{23}$ and Δm_{32}^2 due to the systematic uncertainties.

Table 5.1: **Following copied from the NuMu SA paper:** Sources of uncertainty and their estimated average impact on $\sin^2 \theta_{23}$ and Δm_{32}^2 . Systematic uncertainties are included in a fit to simulated data one at a time via their associated penalty terms. The increase in the one-dimension 68% C.L. interval relative to when only statistical fluctuations are included in the fit is used to estimate the average impact of individual systematic uncertainties. The estimate is obtained by subtracting the 68% C.L. intervals in quadrature, except for the effect of δ_{cp} , where the absolute difference in the size of the intervals is used. The total impact of all sources of systematic uncertainty is obtained by including all systematics in the fit simultaneously, and then adding the effect of δ_{cp} . Simulated data were oscillated with $\Delta m_{32}^2 = 2.66 \times 10^{-3} \text{ eV}^2$ and $\sin^2 \theta_{23} = 0.626$.

Source of uncertainty	Uncertainty in $\sin^2 \theta_{23} (\times 10^{-3})$	Uncertainty in $\Delta m_{32}^2 (10^{-6} \text{ eV}^2)$
Normalization	+5 / -5	+4 / -8
Absolute muon energy scale	+9 / -8	+3 / -10
Relative muon energy scale	+9 / -9	+23 / -14
Absolute hadronic energy scale	+5 / -5	+7 / -3
Relative hadronic energy scale	+10 / -11	+29 / -19
Cross sections and final state interactions	+3 / -3	+12 / -15
$\delta_{cp} (0 - 2\pi)$	+0.2 / -0.3	+10 / -9
Beam background normalization	+3 / -6	+10 / -16
Scintillation model	+4 / -3	+2 / -5
Total systematic uncertainty	+17 / -19	+50 / -47
Statistical uncertainty	+21 / -23	+93 / -99

Table 5.2: Table of uncertainty in $\sin^2\theta_{23}$ and Δm_{32}^2 due to each source of systematic uncertainty when using the standard second analysis. This should be a break down of the table above.

Source of uncertainty	Uncertainty in $\sin^2\theta_{23}(\times 10^{-3})$	Uncertainty in $\Delta m_{32}^2 (10^{-6} \text{ eV}^2)$
Normalisation		
norm	+0 / -0.076	+0.2 / -0
relNorm	+3.6 / -3.1	+3.5 / -6.4
Muon energy scale		
SAMuEScale	+8.5 / -7.9	+2.8 / -10
FDSAMuEScale	+8.7 / -9.2	+23 / -14
muon E scales	+11 / -12	+23 / -20
Hadronic energy scale		
SACalibXY	+5 / -4.7	+4.4 / -1.1
SACalibYFunc	+0.11 / -0.076	+2.4 / -2.9
calibrations	+5 / -4.7	+5.1 / -3.2
SARelHadE	+9.9 / -11	+29 / -19
Cross sections and final state interactions		
TransportPlusNA49	+0.97 / -1.9	+3.7 / -7.1
mecScale	+0.9 / -0.52	+5.5 / -7.1
RPA	+0.68 / -0.55	+1.5 / -2.1
numuSumSmallGENIE	+0.38 / -0.89	+1 / -2.4
MaNCEL	+0.048 / -0.12	+0.28 / -0.51
NormCCQE	+0.41 / -0.42	+1.6 / -1.2
MaCCQEshape	+0.64 / -0.49	+1.7 / -2.4
MaCCRES	+2.2 / -1.5	+8.9 / -12
MvCCRES	+1.4 / -1	+5.4 / -7.1
MaNCRES	+0.4 / -0.82	+1.5 / -2.7
MvNCRES	+0.095 / -0.21	+0.4 / -0.68
CCQEPauliSupViaKF	+0.91 / -0.75	+1.4 / -2.5
GENIE+MEC+RPA	+3.1 / -2.5	+12 / -16
Beam background normalization		
numuNCScale	+3.3 / -6.5	+9.3 / -17
Scintillation model		
SABirks	+3.7 / -3.2	+2.9 / -6.5
osc par	+3.1 / -4	+74 / -2.1
all systs	+15 / -18	+87 / -39

Table 5.3: Table of uncertainty in $\sin^2\theta_{23}$ and Δm_{32}^2 due to each source of systematic uncertainty when splitting the sample into four hadronic energy fraction quantiles and a CVN - remid hybrid selection.

Source of uncertainty	Uncertainty in $\sin^2\theta_{23}(\times 10^{-3})$	Uncertainty in $\Delta m_{32}^2 \left(10^{-6} \text{ eV}^2\right)$
Normalisation		
norm	+0.0455 / -0.0503	+0 / -0.216
relNorm	+5.11 / -5.1	+0.743 / -9.31
Muon energy scale		
SAMuEScale	+2.46 / -1.91	+15.3 / -22.9
FDSAMuEScale	+3.1 / -3.35	+8.01 / -3.69
muon E scales	+3.82 / -3.79	+17.9 / -23.6
Hadronic energy scale		
SACalibXY	+1.53 / -2.09	+14.7 / -17.5
SACalibYFunc	+1.3 / -1.67	+7.96 / -7.22
calibrations	+1.92 / -2.6	+16.2 / -18.5
SARelHadE	+3.15 / -3.39	+8.8 / -4.76
Cross sections and final state interactions		
numuSumSmallGENIE	+0.213 / -0.41	+0.455 / -0.68
MaNCEL	+0 / -0	+0 / -0.216
NormCCQE	+0.726 / -0.95	+2.91 / -2.55
MaCCQEshape	+0.528 / -0.426	+1.6 / -2.92
MaCCRES	+0.706 / -0.143	+11.2 / -14.3
MvCCRES	+0.566 / -0.189	+7.22 / -9.44
MaNCRES	+0.151 / -0.286	+0.616 / -0.833
MvNCRES	+0.0455 / -0.0714	+0.186 / -0.305
CCQEPauliSupViaKF	+0.573 / -0.437	+1.82 / -3.36
TransportPlusNA49	+0.704 / -1.19	+3.14 / -4.25
mecScale	+0.582 / -1.08	+8.97 / -9.7
RPA	+0.298 / -0.16	+2.53 / -3.2
GENIE+MEC+RPA	+1.64 / -1.7	+14.2 / -17.7
Beam background normalization		
numuNCScale	+1.43 / -2.44	+3.67 / -4.23
Scintillation model		
SABirks	+0.193 / -0.739	+12.1 / -14.2
osc par	+2.79 / -4.05	+69.7 / -5.23
all sys	+8.51 / -9.46	+78.8 / -37.8

Chapter 6

Results

ND, FD, Diff hadEFrac spectra (Enu, Emu, Ehad).

Contours, DelChiSqr plots for sin and delM

Chapter 7

Conclusion

Bibliography

- [1] M. V. Diwan, V. Galymov, X. Qian, and A. Rubbia. Long-Baseline Neutrino Experiments. *Ann. Rev. Nucl. Part. Sci.*, 66:47–71, 2016.
- [2] J Chadwick. Distribution in intensity in the magnetic spectrum of the β -rays of radium. *Ver. Dtsch. Physik. Ges*, 16:383–391, 1914. [2](#)
- [3] Wolfgang Pauli. Letter to the physical society of tubingen. *Reproduced in [2]*, 1930. [2](#)
- [4] Enrico Fermi. Tentativo di una teoria dei raggi β . *Il Nuovo Cimento (1924-1942)*, 11(1):1–19, 1934. [2](#)
- [5] Frederick Reines and Clyde L. Cowan. The neutrino. *Nature*, 178:446–449, 1956. [2](#)
- [6] G. Danby et al. Observation of high-energy neutrino reactions and the existence of two kinds of neutrinos. *Phys. Rev. Lett.*, 9:36–44, Jul 1962. [2](#)
- [7] D. Decamp et al. Determination of the Number of Light Neutrino Species. *Phys. Lett.*, B231:519–529, 1989. [3](#)
- [8] S. Schael et al. Precision electroweak measurements on the Z resonance. *Phys. Rept.*, 427:257–454, 2006. [3](#)
- [9] K. Kodama et al. Observation of tau neutrino interactions. *Phys. Lett.*, B504:218–224, 2001. [3](#)
- [10] P. Anselmann et al. Solar neutrinos observed by GALLEX at Gran Sasso. *Phys. Lett.*, B285:376–389, 1992. [3](#)
- [11] Raymond Davis, Don S. Harmer, and Kenneth C. Hoffman. Search for neutrinos from the sun. *Phys. Rev. Lett.*, 20:1205–1209, May 1968. [3](#)
- [12] J.N. Bahcall, N.A. Bahcall, W.A. Fowler, and G. Shaviv. Solar neutrinos and low-energy nuclear cross sections. *Physics Letters B*, 26(6):359 – 361, 1968. [3](#)

- [13] K. S. Hirata et al. Observation of ^8B solar neutrinos in the kamiokande-ii detector. *Phys. Rev. Lett.*, 63:16–19, Jul 1989. [3](#)
- [14] A. I. Abazov et al. Search for neutrinos from the sun using the reaction $^{71}\text{Ga}(\nu_e, e^-)^{71}\text{Ge}$. *Phys. Rev. Lett.*, 67:3332–3335, Dec 1991. [3](#)
- [15] B. Pontecorvo. Neutrino Experiments and the Problem of Conservation of Leptonic Charge. *Sov. Phys. JETP*, 26:984–988, 1968. [*Zh. Eksp. Teor. Fiz.* 53,1717(1967)]. [3](#)
- [16] V. N. Gribov and B. Pontecorvo. Neutrino astronomy and lepton charge. *Phys. Lett.*, B28:493, 1969. [3](#)
- [17] Ziro Maki, Masami Nakagawa, and Shoichi Sakata. Remarks on the unified model of elementary particles. *Prog. Theor. Phys.*, 28:870–880, 1962. [3](#)
- [18] Y. Fukuda et al. Evidence for oscillation of atmospheric neutrinos. *Phys. Rev. Lett.*, 81:1562–1567, Aug 1998. [3](#)
- [19] B. Aharmim et al. Electron energy spectra, fluxes, and day-night asymmetries of ^8B solar neutrinos from measurements with nacl dissolved in the heavy-water detector at the sudbury neutrino observatory. *Phys. Rev. C*, 72:055502, Nov 2005. [4](#)
- [20] C. Patrignani et al. Chin. phys. c, 40, 100001. *Particle Data Group*, 2016. [4](#), [7](#), [8](#), [9](#), [10](#), [19](#)
- [21] R. N. Mohapatra et al. Theory of neutrinos: A White paper. *Rept. Prog. Phys.*, 70:1757–1867, 2007. [4](#)
- [22] K. Eguchi et al. First results from kamland: Evidence for reactor antineutrino disappearance. *Phys. Rev. Lett.*, 90:021802, Jan 2003. [4](#)
- [23] T. Araki et al. Measurement of neutrino oscillation with kamland: Evidence of spectral distortion. *Phys. Rev. Lett.*, 94:081801, Mar 2005. [4](#)
- [24] S. Abe et al. Precision measurement of neutrino oscillation parameters with kamland. *Phys. Rev. Lett.*, 100:221803, Jun 2008. [4](#)
- [25] B. Aharmim et al. Low-energy-threshold analysis of the phase i and phase ii data sets of the sudbury neutrino observatory. *Phys. Rev. C*, 81:055504, May 2010. [5](#)
- [26] B. Aharmim et al. Combined analysis of all three phases of solar neutrino data from the sudbury neutrino observatory. *Phys. Rev. C*, 88:025501, Aug 2013. [5](#)

- [27] J. Hosaka et al. Solar neutrino measurements in super-kamiokande-i. *Phys. Rev. D*, 73:112001, Jun 2006. [5](#)
- [28] K. Abe et al. Solar neutrino results in super-kamiokande-iii. *Phys. Rev. D*, 83:052010, Mar 2011. [5](#)
- [29] F. P. An et al. New measurement of antineutrino oscillation with the full detector configuration at daya bay. *Phys. Rev. Lett.*, 115:111802, Sep 2015. [5](#)
- [30] F. P. An et al. Observation of electron-antineutrino disappearance at Daya Bay. *Phys. Rev. Lett.*, 108:171803, 2012. [5](#)
- [31] J. H. Choi et al. Observation of Energy and Baseline Dependent Reactor Antineutrino Disappearance in the RENO Experiment. *Phys. Rev. Lett.*, 116(21):211801, 2016. [5](#)
- [32] J. K. Ahn et al. Observation of reactor electron antineutrinos disappearance in the reno experiment. *Phys. Rev. Lett.*, 108:191802, May 2012. [5](#)
- [33] Y. Abe et al. Improved measurements of the neutrino mixing angle θ_{13} with the Double Chooz detector. *JHEP*, 10:086, 2014. [Erratum: JHEP02,074(2015)]. [5](#)
- [34] D. G. Michael et al. Observation of muon neutrino disappearance with the minos detectors in the numi neutrino beam. *Phys. Rev. Lett.*, 97:191801, Nov 2006. [6](#)
- [35] P. Adamson et al. Combined analysis of ν_μ disappearance and $\nu_\mu \rightarrow \nu_e$ appearance in minos using accelerator and atmospheric neutrinos. *Phys. Rev. Lett.*, 112:191801, May 2014. [6](#)
- [36] Hiroshi Nunokawa, Stephen Parke, and Jose W. F. Valle. Cp violation and neutrino oscillations. *Prog. Part. Nucl. Phys*, 2007. [7](#)
- [37] P. Adamson et al. First measurement of electron neutrino appearance in NOvA. *Phys. Rev. Lett.*, 116(15):151806, 2016. [9](#)
- [38] D. S. Ayres et al. The NOvA Technical Design Report. *Fermilab Publication*, 2007. [11](#), [14](#), [18](#), [19](#)
- [39] P. Adamson et al. The NuMI Neutrino Beam. *Nucl. Instrum. Meth.*, A806:279–306, 2016. [14](#), [15](#), [16](#)
- [40] Stuart L. Mufson. Scintillator update. *Internal NOvA document, DocDB-8541*, 2013. [21](#)

- [41] John Stuart Marshall. *A study of muon neutrino disappearance with the MINOS detectors and the NuMI neutrino beam*. PhD thesis, Cambridge U., 2008. [29](#)